

## Article

# Analysis of Secondary Controller on MTDC Link with Solar PV Integration for Inter-Area Power Oscillation Damping

Oluwafemi Emmanuel Oni <sup>\*</sup>  and Omowunmi Mary Longe 

Department of Electrical and Electronic Engineering Science, University of Johannesburg, Johannesburg 2006, South Africa; omowunmil@uj.ac.za

<sup>\*</sup> Correspondence: 223248712@student.uj.ac.za; Tel.: +27-11-678984406

**Abstract:** Integration of renewable energy sources is important in limiting the continuous environmental degradation and emissions caused by energy generation from fossil fuels and thus becoming a better alternative for a large-scale power mix. However, an adequate analysis of the interaction with the alternating current (AC) network during network disturbance, especially during inter-area power (IAP) oscillations is needed. Insufficient damping of oscillations can significantly impact the reliability and effective operation of a whole power system. Therefore, this paper focuses on the stability of the modified Kundur two-area four-machine (MKTAFM) system. A robust secondary controller is proposed and implemented on a line commutated converter (LCC)-based multi-terminal high voltage direct current (MTDC) system. The solution consists of a local generator controller and the LCC MTDC (LMTDC) system, voltage-dependent current order limiter, and extinction angle controller. The proposed robust controller is designed for the LMTDC systems to further dampen the inter-area power oscillations. Three operational scenarios were implemented in this study, which are the local generator controller and double circuits AC line, local generator controller with LMTDC controllers, and local generator controller with LMTDC controllers and secondary controller. The simulation result carried out on PSCAD/EMTDC recorded better damping of the inter-area power oscillation with LMTDC. A considerable improvement of 100% damping of the IAP oscillations was observed when a secondary controller was implemented on the LMTDC.

**Keywords:** inter-area power oscillation; two-area four-machine network; solar PV; high voltage direct current; PSCAD; secondary controller



**Citation:** Oni, O.E.; Longe, O.M. Analysis of Secondary Controller on MTDC Link with Solar PV Integration for Inter-Area Power Oscillation Damping. *Energies* **2023**, *16*, 6295. <https://doi.org/10.3390/en16176295>

Academic Editor: Ying-Yi Hong

Received: 22 July 2023

Revised: 26 August 2023

Accepted: 27 August 2023

Published: 29 August 2023



**Copyright:** © 2023 by the authors. Licensee MDPI, Basel, Switzerland. This article is an open access article distributed under the terms and conditions of the Creative Commons Attribution (CC BY) license (<https://creativecommons.org/licenses/by/4.0/>).

## 1. Introduction

An increase in the number of power system interconnections has resulted in inter-area power oscillations, a phenomenon involving groups of generators oscillating relatively to each other that are sometimes hard to control due to their scale and complexity [1]. Being often of low frequency, these oscillations are becoming a big challenge to the safe operation of modern power networks. When poorly damped, inter-area oscillation can further lead to voltage or rotor angle instability, or system collapse. Inter-area oscillations have long been a point of discussion among researchers, power utilities, and industries. The frequency is always in the range of 0.1 to 1 Hz [2]. These oscillations lack damping or are unstable, and when these disturbances take place due to crucial faults on the line, the network becomes less stable.

Engineers and researchers in the power and control systems have worked extremely hard over the past 20 years to increase the stability of power systems [3–6]. The standard controllers, which include the power system stabiliser (PSS), automatic voltage regulator (AVR), and speed governor control, are single-input single-output non-coordinated linear controllers that are mostly not capable of ensuring stability when significant perturbations or contingencies arise. In addition, the AVRs, which are generally employed to maintain the terminal voltage magnitude of the synchronous generator, introduce negative damping

torques, which have a detrimental effect on stability. Because of operating point variations and short circuit disruptions, power systems exhibit electromechanical oscillations. These frequency oscillations must be suppressed to the amount that is acceptable; otherwise, instability might develop as their amplitude grows. In order to address these problems, power system stabilisers (PSSs) are further utilised to produce an extra stabilising signal to the excitation system to dampen these oscillations [7].

Other controllers like the Static Var Compensators (SVC) and flexible AC transmission systems (FACTS) have also been deployed for inter-area oscillations damping; however, under specific operating circumstances, an inter-area mode may be viewable from one area and controllable from another [8,9]. In this situation, a failure or system disturbance in one area will tend to have a greater effect than before in another.

Researchers have developed several efficient techniques to examine the low-frequency oscillation issue [10–12]. Among these, the linearised state matrix's modal analysis offers a fundamental technique for analysing low-frequency oscillations. This approach may be used to identify the system's weakly damped oscillation modes, whether they are local or inter-area. Using linear participation factors, it is possible to pinpoint the high association between a few chosen generators and the weak-damped mode. A fuzzy controller can also be used to provide a fast response and coordinated control of a wide area network for quick damping of inter-area oscillations [13]. In [14], a Fractional Order Proportional Integral (FOPI) was used against the conventional PI controller with an adaptive differential evolution algorithm to further provide an optimal tuning of the FOPI for performance enhancements. Another work also carried out a data-enabled predictive control algorithm on a voltage source converter-based high-voltage DC (HVDC) for optimal damping of wide-area power oscillations [15]. A wide area damping controller (WADC) was proposed for energy storage systems such as capacitors for the damping of low-frequency oscillations [16]. The authors used an accelerated particle swarm optimization technique for the turning of the wide-area controllers. In the related research [17], the authors use dual power oscillation dampers on the active and reactive power of a double-fed induction generator for the damping of the inter-area power (IAP) oscillations.

However, the recent trend and transition towards renewable energy and the deregulation of the electricity market point towards the usage of different DC converter links, which has led to different changes in generation and power transmission patterns as well as grid topology [18]. Therefore, a change is required for a better controller to adequately dampen inter-area oscillations before the generator control goes out of step, especially when operating a thyristor-based multi-terminal HVDC system.

Therefore, this paper presents a novel method to model a multi-terminal line commutated converter (LCC) transmission link to provide a robust, flexible, and expandable oscillation damping for a modified Kundur two-area four-machine (MKTAFM) network. The method used in this paper is to build and validate a secondary controller for one of the rectifying stations of the multi-terminal direct current (MTDC) system. The topology of the secondary controller is first tuned and adjusted precisely for the MTDC network. The LCC-MTDC (LMTDC) grid is equipped with an overall power controller that optimises the power flow and current sharing between the two rectifier stations. Therefore, this paper focused on the control strategy of LMTDC grids in reducing the inter-area oscillation of two-area networks. This control aims to minimise the ripple effect of faults on the AC grid voltage and maintain a power balance in case of a fault in one of the areas.

In the first contribution of this paper, it shows how the stability of two asynchronous grids can be improved. The second contribution of the paper shows how a coordinated control of three-terminal LCC MTDC links can be used to avoid inter-area oscillations interaction between two inter-area modes. The investigation carried out in this study evaluates the performance of an MKTAFM and proffers a better means of inter-area oscillation reduction with the use of some multivariable as well as robust controller designs. Furthermore, this research design handles voltage control and power oscillation damping issues concurrently. Our method is distinguished by the fact that the second level of control

action optimises the performance of the existing control of the rectifier stations and thus improves the performance of the substation. The controller configuration and the parameters required for this implementation are derived methodically from the MKTAFM system model. The suggested secondary control is robust and merges an input–output linearisation control method with a nonlinear control approach. This secondary controller constantly adjusts its parameters in response to changes in working circumstances or structure, thus significantly improving the MTDC controller’s effectiveness.

This paper is structured as follows: the authors first gave an insight into the theoretical analysis of inter-area oscillation utilising a two-machine network. The MTDC model used was then presented alongside the control architectures, which are the main MTDC controllers as well as the secondary controller. The test system modelling and the schematic diagram were then explained. Furthermore, the methodology based on the fault analysis on the test network was given, and the results were then presented. Then, the conclusion section follows, which summarises all the work carried out in this paper.

## 2. Inter-Area Oscillations

Inter-area oscillations, which are oscillations occurring between different regions within a synchronously connected power system, represent the most critical threat to the reliable and stable operation of such a power system [19]. In situations where the conventional control mechanisms, due to either weak tie-lines or inadequate grid strength, are incapable of effectively dampening the system’s oscillations following a disturbance, inter-area oscillation phenomena may arise [20]. The ability of an electrical power system to maintain stability in the face of these minor disturbances is referred to as small-signal stability. In contrast to small-signal perturbations, the nonlinear equations governing power systems can be linearised around a specific steady-state operating condition. Due to the inherent weak damping characteristics of inter-area oscillations, there exists a significant probability of irreversible and extensive blackouts, which can lead to severe economic losses and potential loss of human life, thereby resulting in catastrophic consequences.

The small-signal stability is evaluated using eigenvalue analysis, sometimes referred to as modal analysis. This study is primarily intended to reduce inter-area power oscillations. The theoretical background of the small-signal stability of a power system is further provided in Equations (1) to (5). The synchronous machine’s inertia fluctuations are initially analysed to determine the damping coefficient needed to reduce power system oscillations as effectively as possible. The coefficient of damping signifies the adequate torque needed to control the synchronous speed. Figure 1 [20] gives a schematic of a basic two-area system consisting of two incoherent machines with inertias of the generator denoted by  $H_a$  and  $H_b$  while  $\delta_a$  and  $\delta_b$  indicate the rotor angle of areas A and B oscillating at two distinct frequencies and amplitudes. Equations (1) and (2) give the swing equation for individual machines, which, when subtracted, gives (3). Equation (4) is generated by dividing (3) with the inertia coefficients shortly before the second derivation. Further simplification gives (5). To avoid the complexities of swing equations for numerous synchronised machines during the stability analysis of a large system, all swing equations must be combined to minimise the total amount of iterations needed to produce the final swing equations. The total system equivalent rotating inertia is obtained by adding the rotating inertia  $H$  of each generating unit [21].

$$P_{ma} - P_{ea} = H_a \cdot \frac{2}{\omega} \cdot \frac{\partial^2 \delta_a}{\partial t^2} \quad (1)$$

$$P_{mb} - P_{eb} = H_b \cdot \frac{2}{\omega} \cdot \frac{\partial^2 \delta_b}{\partial t^2} \quad (2)$$

$$\frac{P_{ma} - P_{ea}}{H_a} - \frac{P_{mb} - P_{eb}}{H_b} = \frac{2}{\omega} \cdot \left( \frac{\partial^2 \delta_a}{\partial t^2} - \frac{\partial^2 \delta_b}{\partial t^2} \right) \quad (3)$$

$$\frac{2}{\omega} \cdot \left( \frac{H_a H_b}{H_a + H_b} \right) \cdot \left( \frac{\partial^2 (\delta_a - \delta_b)}{\partial t^2} \right) = \frac{H_b P_{ma} - H_a P_{mb}}{H_a + H_b} - \frac{-H_b P_{ea} - H_b P_{eb}}{H_a + H_b} \quad (4)$$

$$\frac{2}{\omega} \cdot H_{ab} \cdot \frac{\partial^2 \delta_{ab}}{\partial t^2} = P_{abm} - P_{abe} \quad (5)$$

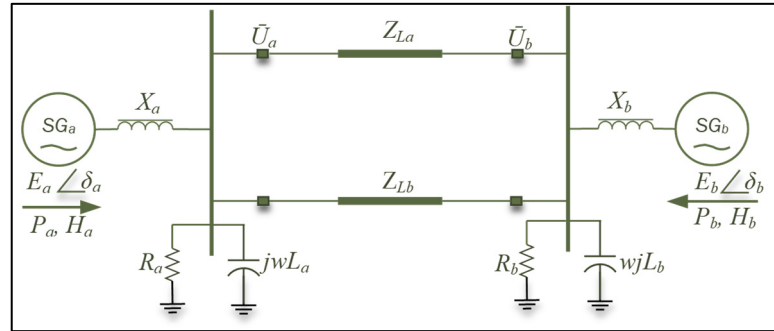


**Figure 1.** Schematic diagram of a two-area network with two machines [20].

The difference in rotor tilt angle between the two generators and the corresponding inertia constant is given as  $H_{ab}$ , and  $\delta_{ab}$  as shown in (6) and (7), respectively.  $P_{mab}$  and  $P_{eab}$  in (8) and (9) are the respective electrical and mechanical power between the two generators. The damping constant  $K_D$  denotes the swing characteristics of the synchronous machine, and it is described using the second-order differential equation in (10). The undamped natural frequency ( $\omega_n$ ) and the damping coefficient ( $\zeta$ ) required to fully reduce the oscillation amplitude are given in (11) and (12), respectively. Since the inertia constant and the oscillation frequency are indirectly proportionate, a power network that is equipped with a high constant of inertia is less prone to faults and vice versa. This demonstrates that the output supplied power has a direct impact on the system's inertia constant. As a result, increasing the stability condition of the power system necessitates an inertia constant value that is greater than 3.5 pu.

$$H_{ab} = \frac{H_a H_b}{H_a + H_b} \quad (6)$$

$$\delta_{ab} = \delta_a - \delta_b \quad (7)$$

$$P_{abm} = \frac{H_b P_{ma} - H_a P_{mb}}{H_a + H_b} \quad (8)$$

$$P_{abe} = \frac{H_b P_{ea} - H_b P_{eb}}{H_a + H_b} \quad (9)$$

$$\frac{2}{\omega} \cdot H_{ab} \cdot \frac{\partial^2 \delta_{ab}}{\partial t^2} + K_D \frac{\partial \delta_{ab}}{\partial t} = -P \cos(\delta_o)_{ab_{max}} \quad (10)$$

$$\omega_n = \sqrt{\frac{\omega P \cos(\delta_o)_{ab_{max}}}{2H_{ab}}} \quad (11)$$

$$\zeta = \frac{1}{2} K_D \sqrt{\frac{\omega}{2P \cos(\delta_o)_{ab_{max}}}} \quad (12)$$

### 3. System Model

#### 3.1. Test Network Modelling

The system under investigation in this research paper is a network, depicted in Figure 2. It comprises four synchronous generators situated in two distinct areas, a 50 MW grid-tied solar PV connected at BB2, and a three-terminal line-commutated multi-terminal direct current (LMTDC). The synchronous generators employed in this study are equipped with an IEEE AC4A exciter for automatic voltage regulation (AVR) and an IEEE single-input power system stabiliser (PSS). To introduce a significant line impedance, the transmission line linking BB10 to BB11 was modified, increasing its distance from 25 km to 80 km. Consequently, a double-circuit transmission line was utilised to enhance the power transfer between area 1 and area 2. Subsequently, a real-time domain modelling and simulation approach is employed to analyse the complete generator's inter-area power and frequency oscillations. Two system faults are simulated to represent a worst-case scenario. The power output, synchronous speed, and inter-area power transmission of each generating unit are plotted during these system disturbances. Bus BB7, BB8, and BB9 are selected for power transfer quality analysis at these locations and to verify the voltage profile. This mode is classified as inter-area since it involves two coherent sets of generators oscillating at a low frequency in opposition to each other.

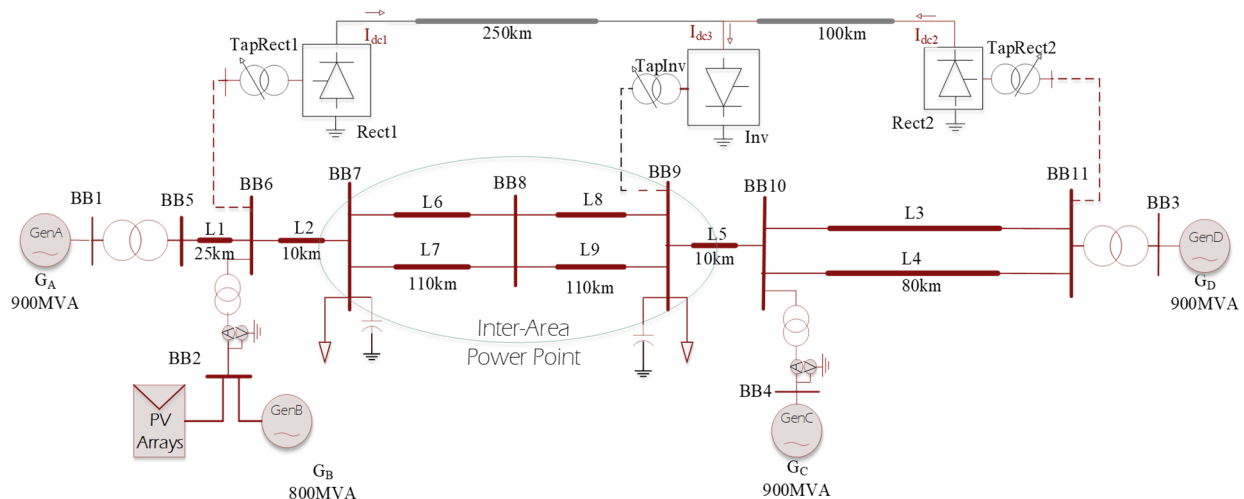


**Figure 2.** The Kundur two-area four-machine network.

Power Systems Computer Aided Design (PSCAD) was used to model the synchronous machines, which included the IEEE controller model for the AVR and the PSS. All generators were evaluated in terms of the true inertial constant and were linked together by a step-up transformer of 20/230 kV voltage range and an apparent power rating of 900 MVA. During the evaluation time, a constant value was pre-selected for the governor control for all four machines to obtain an in-depth impact of the DC controller, AVR, and PSS effects on minimising the disturbances caused by the fault on the complete model. The authors in [2,20,22] gave an explanation about the modelling of these machines and further provided the parameters for both the generators and the transformers and the line models.

In the dynamic simulation of this network, three operational scenarios were considered: (1) usage of only the AC line on the MKTAFM network; (2) usage of LMTDC link to interconnect bus BB6 (rectifier 1) or BB11 (rectifier 2) to the inverter station at bus BB9; and (3) implementation of a secondary controller on the rectifier 1 station. During the second and third scenarios, a single circuit was used rather than the double circuits shown in the MKTAFM network. This measure was taken to avoid excessive power transfer across the bus and to also show the scenario of replacing an existing AC line with DC lines, thereby showing the impact of it on the overall system.

The power system's dynamic characteristics are captured by the collection of nonlinear differential algebraic equations, which serve as the mathematical representation of the system. Equations (13)–(15) express these dynamics' analysis of the power system interconnections.

$$\dot{x} = f(x, y, u) \quad (13)$$

$$0 = g(x, y, u) \quad (14)$$

$$z = h(x, y, u) \quad (15)$$

The vector  $x$  in these equations represents the state variables, the vector  $y$  represents the algebraic variables, the vector  $u$  represents the input variables, and the vector  $z$  represents the output variables. These equations regulate the dynamic behaviour of the many types of models used in this study. The specific equations relating to the dynamic behaviour of these models are discussed in the following sections.

### 3.2. Grid-Tied Solar PV Analysis

A single solar PV source is a proportionate equivalent of several strings of PV modules connected in parallel with each of the string modules connected in series. With identical arrays of PV modules, a general analysis can be given for a single model solar cell as shown in Figure 3 using the electrical equivalent circuit [23,24]:

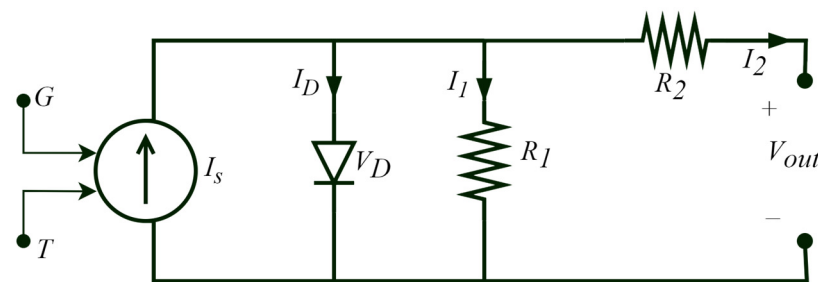


**Figure 3.** Solar PV cell model.

The generated photocurrent, denoted as  $I_s$ , in a photovoltaic (PV) cell exhibits a linear relationship with the solar irradiance it is exposed to from sunlight. However, the presence of the anti-parallel diode results in non-linear current-voltage (I-V) characteristics of the PV cell. By applying Kirchhoff's current law to the circuit, (16) is obtained. Equation (18) is derived by substituting the relevant expressions for the diode current ( $I_D$ ) and the shunt branch current ( $I_1$ ). The modified non-ideal factor, expressed in (18), is directly proportional to the temperature of the cell, denoted as  $T_c$ . The photocurrent, as described in (19), is dependent on the solar radiation ( $G$ ) incident on the PV cell's surface and the cell temperature ( $T_c$ ). The short circuit current ( $I_{SCR}$ ) is defined with respect to a reference solar radiation ( $G_R$ ) and a reference cell temperature ( $T_R$ ). The parameter  $\alpha T$  represents the temperature coefficient of the photocurrent, with a value of  $\alpha_T = 0.0017$  A/K for silicon solar cells. The dark saturation current ( $I_0$ ), given by (20), is influenced by the cell temperature, where  $I_{0R}$  represents the dark current at the reference temperature. In these equations,  $q$  denotes the charge of an electron,  $k$  represents the Boltzmann constant, e.g., corresponds to the band-gap energy of the solar cell material, and  $n$  is the ideality factor when  $kTc = q$ . The instantaneous values of solar radiation ( $G$ ) and the operating temperature ( $T$ ) of the cell are measured in watts per square meter ( $W/m^2$ ) and degrees Celsius ( $^{\circ}C$ ), respectively.

Considering that a PV module comprises numerous cells connected in series, and a PV array consists of both series and parallel combinations of modules, the circuit model of a single cell can be scaled up to represent any desired series/parallel configuration.

$$I_s = I_D + I_1 + I_2 \quad (16)$$

$$I_2 = I_s - I_o \left( e^{\frac{V_{out} + I_2 R_2}{m}} - 1 \right) - \left( \frac{V_{out} + I_2 R_2}{R_1} \right) \quad (17)$$

$$m = \frac{nkT_c}{q} \quad (18)$$

$$I_s = I_{SCR} \cdot \left( \frac{G}{G_R} \right) \cdot [1 + \alpha_T (T_C - T_R)] \quad (19)$$

$$I_o = I_{oR} \cdot \left( \frac{T_C}{T_R} \right)^3 \cdot e \left[ \frac{q e_g}{nk} \left( \frac{1}{T_R} - \frac{1}{T_C} \right) \right] \quad (20)$$

### 3.3. PV Modelling

The schematic diagram presented in Figure 4 illustrates the comprehensive configuration of a grid-connected photovoltaic (PV) model consisting of DC–DC and DC–AC converters block diagram within it (parameter details in Appendix A). The components encompassed in this scheme include PV arrays, a DC–DC boost converter, a voltage source converter for DC–AC conversion, and an AC filter. The PV subsystems are capable of functioning in two primary modes, namely, continuous conduction mode (CCM) and discontinuous conduction mode (DCM). In solar PV applications, the CCM is the preferred mode of operation [25].

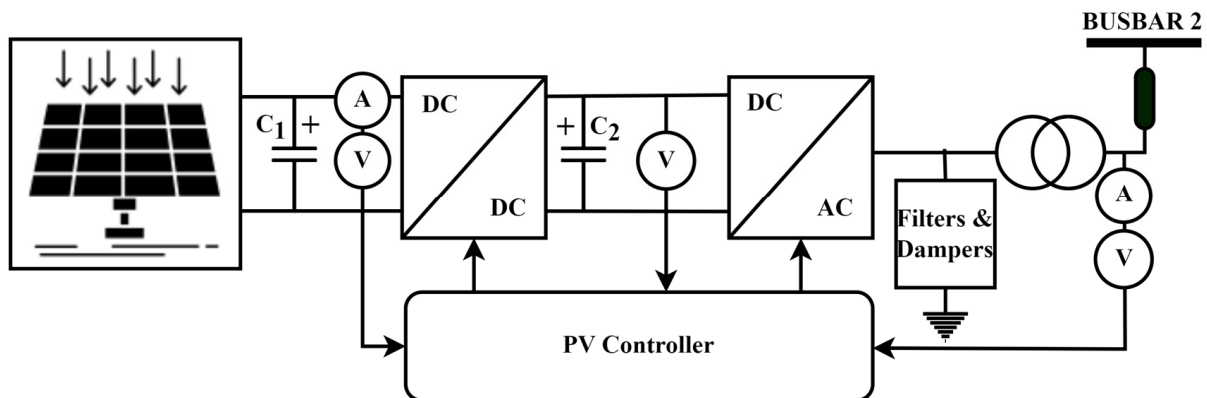


Figure 4. Grid-tied PV model.

The PV system in this study utilised a DC–DC boost converter model as shown in Figure 4. It serves as a step-up converter extensively employed for integrating low-voltage PV modules with the utility grid. Furthermore, it fulfills the role of maximum power point tracking (MPPT) under nominal utility conditions. In the boost converter, the voltage is increased by adjusting the duty cycle. The DC–DC converter plays a vital role in a solar PV application by transforming the input direct current from one voltage level to the required level. It serves as a crucial component for maximum power point (MPP) tracking. The operation of the DC–DC converter serves as the foundation for detecting the MPP, as outlined in the proposed global MPPT control algorithm. In practical scenarios, despite the implementation of MPPT, the output voltage of a PV string remains significantly low. Therefore, a front-end DC–DC converter with step-up capability is necessary for grid connection. The fundamental principle behind the MPPT algorithm relies on harnessing the voltage and current variations resulting from instantaneous power fluctuations. By analysing these variations, it becomes possible to determine the power gradient and assess whether the solar PV system is operating near the maximum power point. The maximum power delivered by the solar PV array is the product of the optimal operating voltage and current of the PV array at the maximum power output condition.

To achieve grid synchronisation, an inverter is necessary. The control of the inverter governs the power and frequency on the AC side while minimising system harmonics.

The switches within the inverter are controlled through the implementation of an inverter control algorithm [26].

### 3.4. MTDC Design

The standard control approach of LMTDC converters requires rectifier stations to be in DC current control (DCC) mode. Voltage-dependent current order limiter (VDCOL) and current control are further used to provide a better current order control. As shown in Figure 5, the DCC method is used at the rectifier 1 substation. The current order is generated by either selecting the reference input current deployed by the overall power controller or by selecting the current order from the VDCOL. The VDCOL gets its input from the intended filtered DC current ( $I_{drect1}$ ) measured from the DC line. The lower value of any of the two is chosen as the standard current order ( $I_{ord}$ ) for the generation of the firing angle for the rectifier. The same process is used at the rectifier 2 substation as illustrated in Figure 6. The difference between the rectifier 1 and the rectifier 2 controller is that the rectifier 1 substation has another current order input from the secondary controller (SC). Also, both rectifiers have different power-carrying capacities and are thus rated differently in the parameters that are used for their control signals.

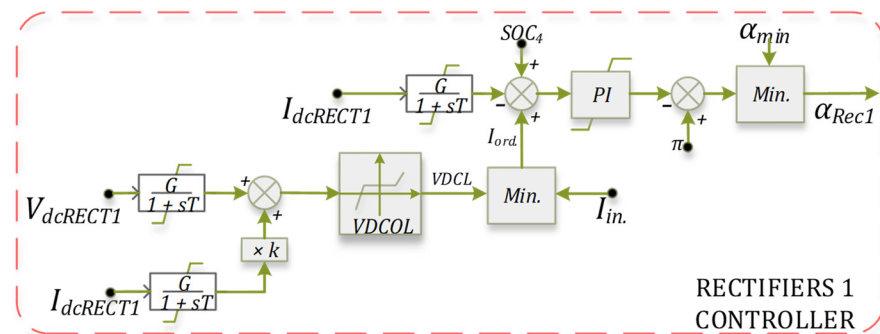


Figure 5. LMTDC rectifier 1 control diagram.

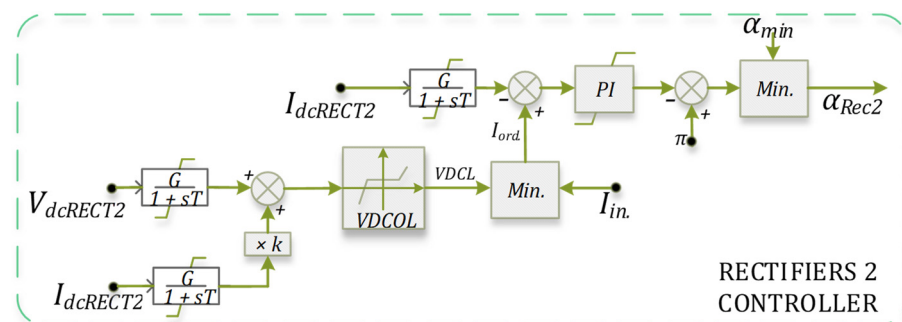


Figure 6. LMTDC rectifier 2 control diagram.

Various control approaches can be used to regulate the inverter, including extinction angle control (EAC), DCC, and DC voltage control (DVC). The reference signal is acquired in the same manner as in the rectifier control mode as shown in Figure 7. However, unlike the rectifier’s DCC, the inverter’s DC current is limited to the difference between the amount of the standard current order and that of the current margin ( $I_{marg}$ ). In other to positively influence the power reversal process, the current margin is programmed into the inverter current control and normally set on a fixed range of 0.1–0.15 pu. A current error control (I-error) indication is commonly used between the DCC and the DVC. This generated I-error can also be inserted between the DCC and the EAC to smoothen changes between the control modes. The smallest of these generated parameters is chosen as the inverter control parameters because it is preferable to run the inverter at the smallest extinction angle possible to reduce the power losses, reduce the amount of reactive power needed to compensate for the thyristor valve, and, ultimately, reduce the harmonic distortion content.

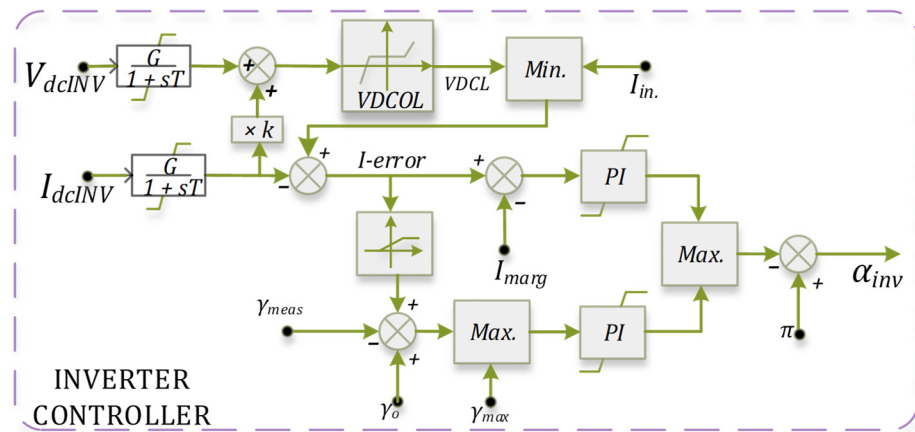


Figure 7. LMTDC inverter control diagram.

For every input of this control signal, being in per unit, it must undergo a first-order inertia transfer function to make the control switching process a smooth transition. The equation is expressed as follows:

$$\left( G_1 \frac{1}{1 + sT_1} \right) \tag{21}$$

The LMTDC system’s fault vulnerability is entirely dependent on its general coordination; thus, each converter’s controllers were preset and adjusted to fit the case study. The overall power controller regulates and oversees the LMTDC link’s converter operations. It accepts a varying power order measured from the systems. This controller yields the current order after being divided by the measured DC voltage by guaranteeing that the total DC current of all converters is zero ( $I_{dc} = 0$ ). The master control, seen in Figure 8, is responsible for balancing the combined converter’s power and current order. This controller generates the current order for each converter system based on the measured voltage at each converter station and a preset power order. It also provides allowance and compensation in case of DC line losses.

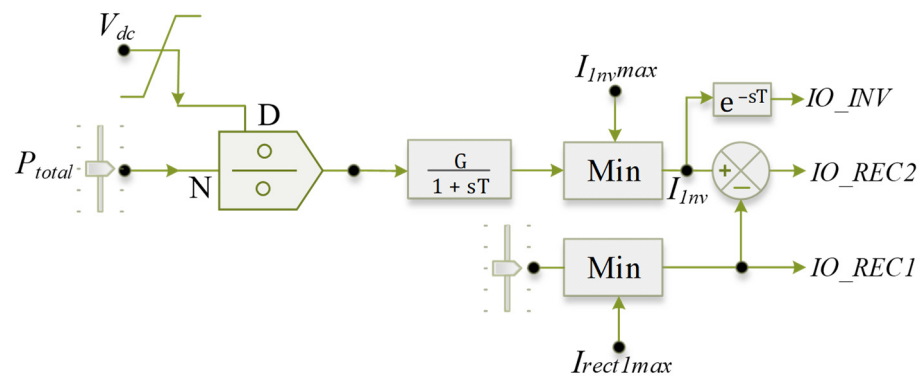


Figure 8. Overall power controller.

The LMTDC used in this study comprises a three-terminal thyristor converter. The firing angle at rectifiers and converter units is used to regulate the DC voltages. The overall power controllers generate the input value of the DC current for each of the converter’s stations. The DC voltage for the rectifier and inverter stations, as well as the rectifier firing angle, are expressed below [27–29]:

$$V_{dr} = 3.12BTU \cos \alpha - 0.96BX_c I_{dc} \tag{22}$$

$$V_{di} = 3.12BTU \cos \beta + 0.96BX_c I_{dc} \tag{23}$$

$$\alpha_c = \cos^{-1} \left( \frac{U_{dc} + I_{dcref} R_{dc} + 0.955 B X I_{dcref}}{3.1213 \cdot BTU} \right) \tag{24}$$

The subscripts *r* and *i* in the (22) to (23) stand for rectifier and inverter. The rectifier and inverter DC voltage are denoted as  $V_{dr}$  and  $V_{di}$ , while the RMS L-L converter voltage is shown as  $U$ . The number of series-connected bridges of the thyristors is denoted by  $B$ . Therefore, for a 12-pulse thyristor converter,  $B = 2$ ; meanwhile, a bipolar HVDC system will have a  $B$ -value of four. The firing angle ( $\alpha$ ) in (24) is the required angle at which the converter gets turned on and begins to conduct;  $X$  denotes the commutation reactance, and  $R_{dc}$  is the total resistance at the DC side of the converter. Also,  $T$  stands for the transformer ratio, and the AC voltage as each of the converter stations is depicted as  $U$ .

The classic secondary controller (SC) adopted in this study is like the power oscillation damper that has the same mode of construction as a generator’s PSS (power system stabiliser), which includes a washout filter, a gain  $G$ , and ‘ $p$ ’ phase lead-lag blocks (Figure 9). The transfer function provided in (25) defines the secondary controller equations with the parameter details in Table 1. The washout filter is typically used as a link between the measured signal and the used signal in the control loop to washout (or reject) the steady-state component of the measurements while passing the transient ones. The traditional parametric tuning method comprises two steps: (i) the calculation of  $T_4$  and  $T_5$  to adjust the phase of the mode’s residue to  $180^\circ$  and (ii) the adjusting of the gain  $G$  to achieve the required damping. The output control signal from each of the transfer functions during the simulation of the whole system is plotted in Figure 10.

$$H_{soc} = \left( G_1 \frac{1}{1 + sT_1} \right) \cdot \left( G_2 \frac{sT_2}{1 + sT_3} \right) \cdot \left( G_3 \frac{1 + sT_4}{1 + sT_5} \right)^n \cdot \left( G_4 \frac{1}{1 + sT_6} \right) \tag{25}$$

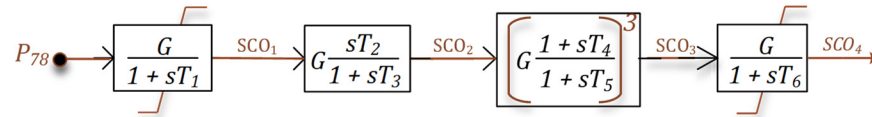


Figure 9. Secondary controller block diagram of the proposed model.

Table 1. Optimised parameter values.

| Model       | Parameter              | Value                                  |
|-------------|------------------------|--|
| SC Gain     | G1, G2, G3, G4,        | [0.006; 0.31; 1.01; 0.24]              |
| SC Time (s) | T1, T2, T3, T4, T5, T6 | [0.012; 1.5; 1.5; 0.514; 0.172; 0.055] |

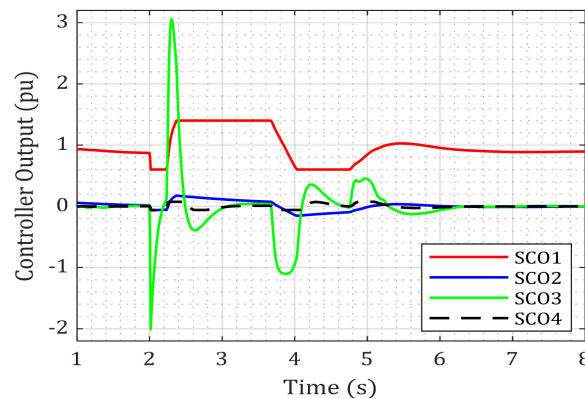


Figure 10. Measure control input during the simulation of the secondary controller.

#### 4. Methodology and Scenarios

To study the small-signal characteristics of an MKTAFM network during the integration of solar PV systems, a dynamic RMS simulation was performed on PSCAD/EMTDC, a

power systems simulation software designed for the simulation of electromagnetic transient analysis of DC networks. The base case study, which is termed the first scenario of using only the AC lines and solar PV, was first analyzed. The simulation included a fault analysis where a three-phase-to-ground (3Ph-G) fault occurred on the L7 line connecting BB7 and BB8, with a fault clearing time of 210 ms and a disturbance of 1.2 s on GenC. Both events happened concurrently at the 2.0 s mark time during the simulation, thus affecting different areas of the system to truly test the limits of the power system operation. The chosen disturbances simulated signify a worst-case scenario. The second scenario recorded a few changes, as three of the transmission lines, L4, L7, and L9, were replaced with DC lines (see Figure 2), but the same fault impedance was applied to the system when it was connected to the LMTDC link. The same situation applies to scenario 3 with LMTDC lines; however, it differs in the inclusion of the secondary controller for the quick damping of the inter-area power oscillation.

In all the scenarios covered in this study, the power generated by GenB and the solar PV link never changes, as shown in Figure 11, with GenB and the solar PV recording an active power of 622 MW and 50 MW, respectively. The goal of this study is to evaluate the controller contribution of LMTDC in reducing inter-area power oscillations even during a high penetration of renewable energy.

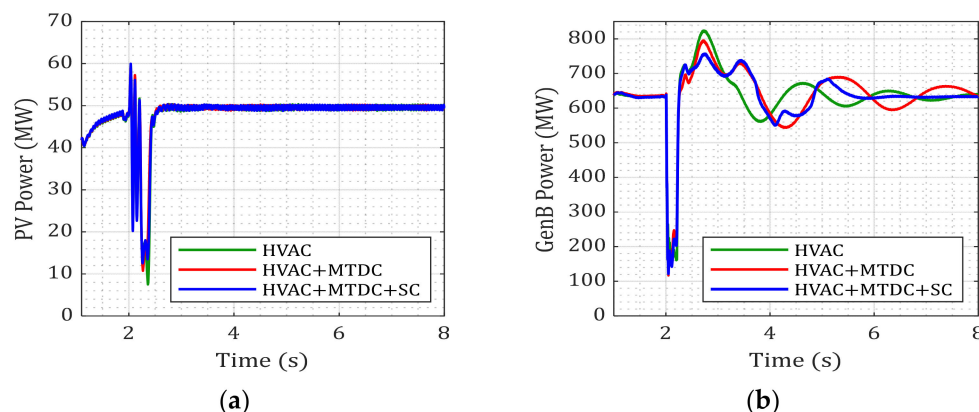


**Figure 11.** Active power for (a) solar PV, and (b) GenB.

## 5. Results

The results of the dynamic analysis using PSCAD/EMTDC simulation tools consisted of observations of the generator's active power, oscillation speed, and converter data. The magnitude and damping rate of the oscillation were studied for both situations for the inter-area power oscillation. The generator speed also provides information about the contributing element for each generator in the oscillatory phases. Since the focus is on the inter-area oscillation, the system short circuit fault time was limited to a short period of 210 ms. After these system disruptions, a positive damping coefficient was recorded during all scenarios, i.e., the systems maintained their pre-fault steady state condition, albeit with distinct amplitudes and waveform distortion.

The plot shown in Figure 12 is the active power for all the generators in the three scenarios. In the first scenario, the synchronous machine 2 (GenB) power dips lowest to a 201 MW value at the instant of the 3Ph-G fault occurrence; GenA follows thereafter. This dip in GenB is due to the near proximity to the transmission line fault following a decline in the active power produced by GenC due to a protracted generator disruption nearing 1 s simulation time on GenC. The active power recorded on this generator reached 916 MW, nearly 1.4 pu of its operating state value, due to the increase in the accelerating power after being subjected to a fault. Another observation in this plot is the inaccuracy in the power generated in each generator due to the high line impedance and losses on each of the AC lines used. Furthermore, GenD generated the largest share of the load power, followed by GenB, GenA, and then GenC. This disparity is caused by the high line impedance between

GenC and the load area. This points to the fact that even the inclusion of the solar PV link is still not sufficient to provide an adequate damping torque that can sufficiently dampen the power oscillations.

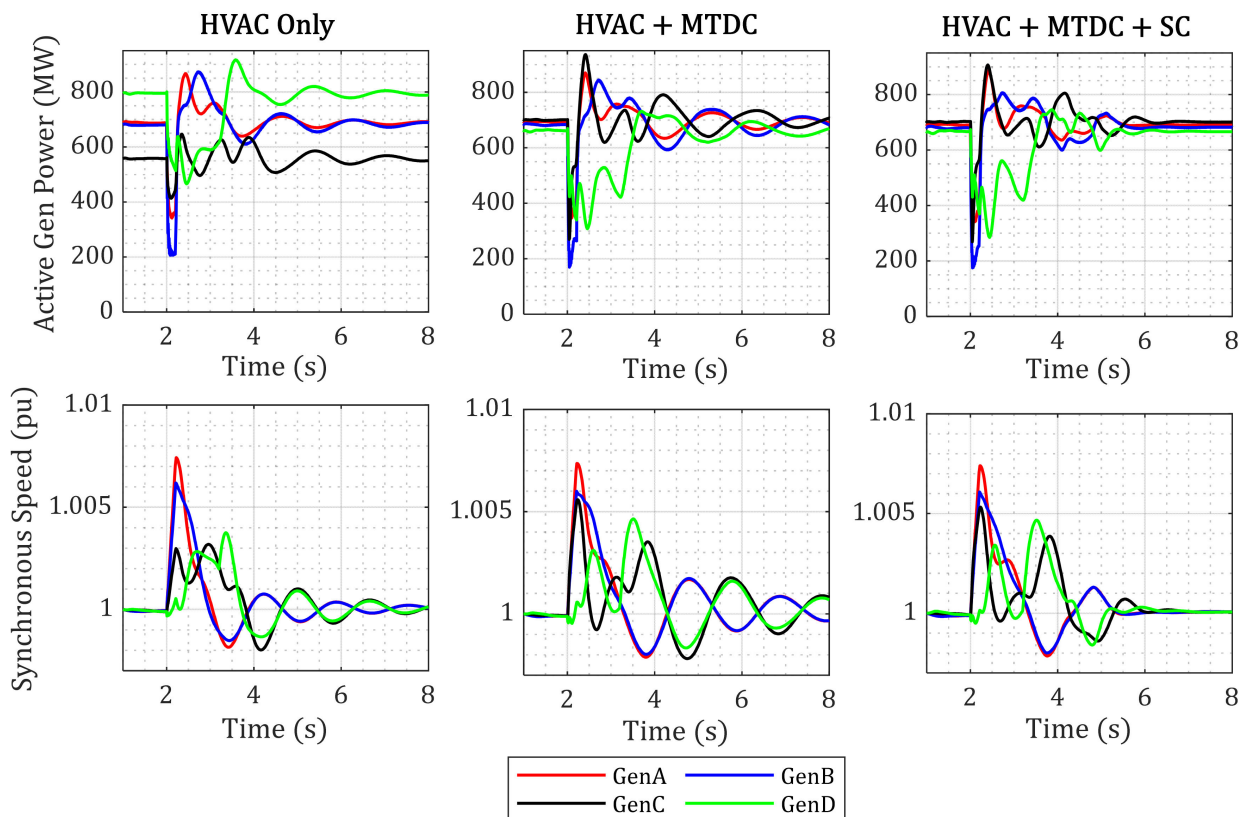


**Figure 12.** Active power and synchronous speed plot.

The second scenario involves the replacement of all the double transmission circuits in the system with a single transmission line and DC lines, with the DC lines forming a three-terminal DC (LMTDC) link. A performance comparison was carried out with regards to the first case study to determine which links achieved better inter-area oscillation reduction and to investigate if the LMTDC link can damp oscillation generated by solar PV during system disturbance. In Figure 12, the active power shown in this plot exhibited a close-to-average power generation. This close range of power transfer is due to the benefits offered by the LMTDC system in loss reduction and enhancement of power transfer. Therefore, after the 3Ph-G fault, due to a continuous generator fault, GenD and GenC registered the greatest power amplitude of 916 MW. These amplitudes resulted in greater inertia value in recovering the normal operating point of the complete network. GenB still recorded the lowest dip of 175 MW. However, a better power profile can be seen in this plot as all four generators recorded a close range of power. The functionality of this was made possible with the inclusion of the LMTDC link, which further helped in the active power dispatch. However, the simulation plots at this stage still contain a number of oscillations. The inclusion of the secondary controller to the rectifier 1 station totally eradicated these oscillations at 5.8 s simulation time.

Figure 12 shows the frequency swings of the generators that were observed in the system. This result comprises incoherent machines, with area A having a different inertia constant compared to area 2. This results in the generators in area A swinging with the machines in area 2. The highest oscillatory modes, up to 1.007 pu, were observed in the GenA and GenB subplots. The machine's accelerating power played a role in meeting the expected load demand in area B, which led to the maintenance of a stable operating state, albeit with a high oscillating frequency. During the first two scenarios, the generators'

power system stabiliser (PSS) and automatic voltage regulator (AVR) controllers had already provided damping torque to maintain stable operating points. However, this was insufficient in quickly generating a damping coefficient that would adequately and effectively return the entire test network to its steady-state operational state. An increase in the fault clearance time ( $t_c = 300$  ms) would result in system collapse, where the systems can no longer maintain a stable operating point. In Figure 12, the synchronous speed for GenC and GenD both followed the same pattern of system oscillation being similar in area 2; the same applies to GenA and GenB in area 1.

In the third scenario, although initial oscillation is the same as the previous scenarios, the inclusion of the secondary controller into the KMTAFM network generated a quick damping torque for the system to quickly return to its steady state condition.

Following the fault, BB7, BB8, and BB9 in Figure 13 illustrate the bus voltages during the three scenarios. In order to fully understand the comparison between the three different scenarios based on the voltage profile, the busbar voltage was grouped together, indicating a particular bus voltage for the three different scenarios. The observation of these voltage profiles shows that BB8 is the weakest bus in the network across all three scenarios, which can be attributed to its distance from the generating plants in both areas. BB7 followed as the second weakest bus. However, the second scenario recorded a better voltage profile than when only HVAC and solar PV were used. The plot also indicates that an increase in transmission distance between BB10 and BB11 did not have a significant impact on BB9's voltage profile in contrast to the other buses examined in both scenarios. During the third scenario, the oscillations observed in the system voltage profile were completely improved, and the system's steady conditions were stabilised after approximately two cycles (5.8 s of simulation time).

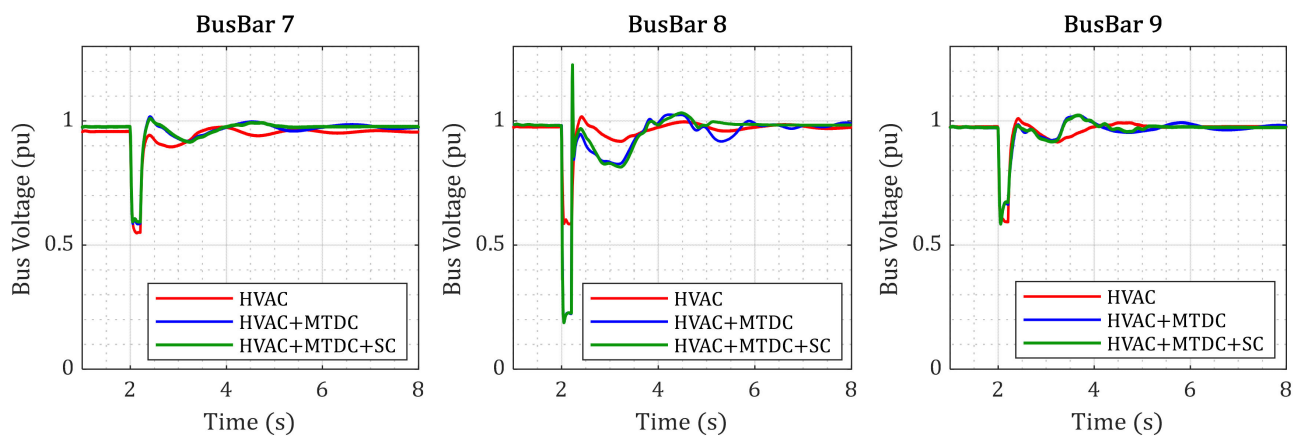
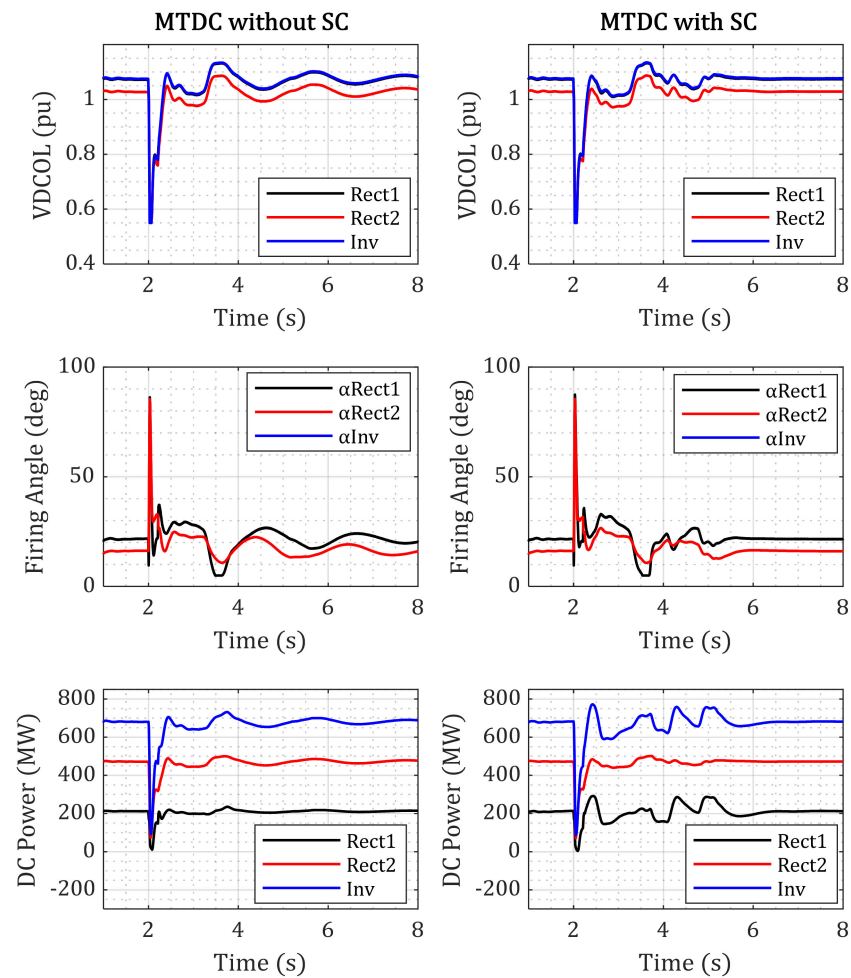


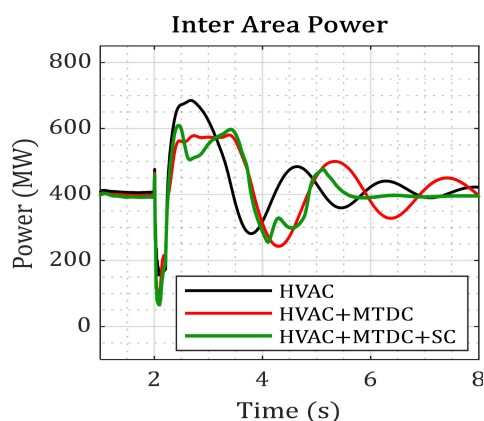
Figure 13. Bus voltage profile.

Figure 14 shows the impact of the LMTDC in reducing the oscillation after the system's disturbance. The plot was categorised into two parts, depicting the scenario with and without the secondary controller. The voltage-dependent current order limiter has a look-up graph based on the V-I characteristics of the converter that helps the converter in reducing the amount of current that flows through the link when the voltage reduces. By doing this, the converter reduces the amount of power that flows through the link during this disturbance and thus reduces the amount of reactive power consumption. The current output from the VDCOL is passed through a PI controller that further generates the firing angle for each of the converters. The scenarios without the inclusion of the secondary controller recorded a ripple that was still very much visible at the end of the simulation time. These oscillations are still further cumulated into the firing angle for each of the converters. The inclusion of the secondary controller created an immediate ripple that further provided a quick, sufficient, and robust damping torque in totally eradicating the oscillations in the current output from the VDCOL and further provided a better firing angle, and thus a better DC power output.



**Figure 14.** LMTDC converter plots.

Figure 15 demonstrates the inter-area power transfer between BB7 and BB9. The study revealed that without the presence of MTDC links, the inter-area power oscillations had a slow damping rate during the initial scenario, where only AC transmission lines were used. During the post-fault transient condition, the two areas in the study system contributed more to the oscillations, which delayed the system from reaching a steady-state condition. However, the addition of the MTDC link showed that the damping rate of the inter-area power oscillations increased significantly during the same disturbance scenario. The amplitude of the IAP transfer likewise showed a considerable positive damping rate, leading to a more stable operative condition. However, not all the inter-area oscillation was fully damped at the 8 s simulation time. Therefore, a secondary controller was further used. The result from this analysis shows a better oscillation damping, whereby all the oscillation was completely damped at exactly 5.8 s simulation time. During this scenario, the active power transfer comprised the power transmitted from the AC line L6 to line L8 and the DC power transmitted through the rectifier 1 converter link. The plot indicates that the damping ratio resulted in a complete suppression of the oscillation amplitude's value during the second period of simulation.



**Figure 15.** Inter-area power oscillation.

#### Performance Comparison

In this section, a comparison of various schemes, presented in Table 2, is conducted to assess the contributions of the proposed model and controllers. The highlighted reviews are based on authors who carried out inter-area power oscillation studies using the two-area four-machine (TAFM) network.

**Table 2.** Performance comparison of the proposed model.

| Ref     | Method   | Performance in Comparison to This Study   |
|---------|--|---|
| [30]    | Adaptive online control design for a power system stabiliser (PSS) and comparing the classic PSS controller and an online tuned PSS.   | The results based on the 3Ph-G faults show little impact as both the classic and the online tuned PSS recorded some amount of oscillation even at 10 s simulation time.                         |
| [31]    | They used weighted signals representing different areas to optimize a PSS. They used two optimization methods: the Harmony Search (HS) algorithm and the Teaching Learned Based Optimization (TLBO) technique. | The TLBO with the PSS provided a quick settling time of the bus voltage oscillation and recorded a settling time of 4.8 s, but fails to include the dynamics of HVDC/MTDC lines on the systems. |
| [32,33] | They used VSC HVDC power oscillation dampers (POD), PSS, and wide area measurement signals-based controllers designed with a novel linear quadratic gaussian (LQG) method.                                     | The result utilising LQG POD provided a better oscillation reduction technique. However, the time taken to reach a total settling phase is around 12 s.   |
| [34,35] | These literatures used an enhanced static synchronous compensator to damp inter-area power oscillation and also compared different FACTS devices.  | The result shows an improved power oscillation; however, at a longer simulation time of $\cong 10$ s. It also differs from the present study as no MTDC link was used.                          |
| [36–38] | They used a single thyristor controlled braking resistor and dual fuzzy logic for the minimization of inter-area power oscillation.  | A reduced oscillation was recorded, but the 3-phase fault on the line generated a prolong oscillation.  |
| [39,40] | They used a clustering distributed generator to provide more reserves for generators. They also used a phase wide area measurement for the control.  | They recorded a quick settling time, but the DGs in the load bus provided a quick supply to the load. An MTDC link was not included.  |

## 6. Conclusions

The small-signal stability of two incoherent machines is one of the biggest problems facing power utilities. Further problems also arise during the integration of renewable energies, especially solar PV with high levels of intermittencies. Therefore, in this study, a secondary control technique that utilises a hierarchical control structure to enhance the damping of inter-area oscillation stability was introduced. The solution is multi-faceted, consisting primarily of the local controllers, voltage and rotor speed regulator, a centralised

power controller for the LMTDC, and a current and extinction angle controller for the LMTDC model. These joint controllers were added to maximally improve the system performance. Firstly, a dynamic simulation model of an MKTAFM network was developed (first scenario). In the second scenario, a generator disturbance at GenD and a 210 ms 3Ph-G fault on the transmission line (L6) linking BB7 to BB8 were considered, with both faults occurring at 2 s simulation time. In the third scenario, the system response consisting of the details of the generators was monitored on a plot, and the times at which the system experienced a highly imbalanced waveform were obtained, as well as the time taken for the generator control to sufficiently dampen the system's oscillations. Afterwards, a study case involving the replacement of the double transmission lines on the network with an LMTDC system (second scenario) was implemented. A secondary control was further added to the LMTDC (third scenario). Finally, a nonlinear time-domain dynamics analysis was carried out on the LMTDC network, and the generator and the bus voltage profile were monitored.

Following the 3Ph-G fault on the test network, the poorest damped modes in each grid scenario being observable confirmed that the implementation of the secondary controller on the LMTDC provided a 100% damping of the oscillation at exactly 5.8 s simulation time with zero rates of change of the amplitudes compared to the first and second scenarios. The same is seen in the inter-area power transfer between BB7 and BB9, which initially recorded a continuous oscillation due to insufficient damping torque. The findings thus show that the proposed novel controller is durable, significantly raises the stability limit of the entire system, and improves the performance of primary controllers.

Further research will be conducted to reduce the sensitive response of the controller to large and non-uniform transmission delays and its impact if added to other LMTDC substations. Another point of focus is also to reduce the transient increase in the firing angle of the LMTDC converters during faults.

**Author Contributions:** Conceptualization, O.E.O. and O.M.L.; methodology, O.E.O. and O.M.L.; software, O.E.O.; validation, O.E.O. and O.M.L.; formal analysis, O.E.O. and O.M.L.; investigation, O.E.O. and O.M.L.; resources, O.E.O. and O.M.L.; data curation, O.E.O. and O.M.L.; writing—original draft preparation, O.E.O. and O.M.L.; writing—review and editing, O.E.O. and O.M.L.; visualization, O.E.O. and O.M.L.; supervision, O.M.L.; project administration, O.M.L.; funding acquisition, O.M.L. All authors have read and agreed to the published version of the manuscript.

**Funding:** This research received no external funding.

**Data Availability Statement:** No data was created.

**Conflicts of Interest:** The authors declare no conflict of interest.

## Appendix A

**Table A1.** Solar PV system specifications.

| Parameter                            | Value  |
|--------------------------------------|--------|
| Maximum power                        | 250 W  |
| Short-circuit current per cell       | 2.5 A  |
| Current at maximum power point       | 2.0 A  |
| Temperature coefficient of $I_s$     | 0.001  |
| Modules connected in series per      | 35     |
| Modules connected parallel pers      | 11,000 |
| Cells connected in series per module | 35     |
| Reference radiation                  | 1010   |
| Reference cell temperature           | 29     |
| Diode Ideality factor (m)            | 1.5    |
| PV system rating/system base         | 50 MW  |

## References

1. Sitompul, S.; Fujita, G. In Impact of State-of-Charge Control Integrated with Load-Frequency Control on Battery Energy Storage System in Islanded Microgrid System. In Proceedings of the 2021 IEEE 12th Energy Conversion Congress & Exposition-Asia (ECCE-Asia), Singapore, 24–27 May 2021; pp. 199–203.
2. Klein, M.; Rogers, G.J.; Kundur, P. A fundamental study of inter-area oscillations in power systems. *IEEE Trans. Power Syst.* **1991**, *6*, 914–921. [[CrossRef](#)]
3. Machowski, J.; Lubosny, Z.; Bialek, J.W.; Bumby, J.R. *Power System Dynamics: Stability and Control*; John Wiley & Sons: Hoboken, NJ, USA, 2020.
4. Ufa, R.; Rudnik, V.; Malkova, Y.; Bay, Y.; Kosmynina, N. Impact of renewable generation unit on stability of power systems. *Int. J. Hydrogen Energy* **2022**, *47*, 19947–19954. [[CrossRef](#)]
5. Tina, G.M.; Maione, G.; Licciardello, S. Evaluation of Technical Solutions to Improve Transient Stability in Power Systems with Wind Power Generation. *Energies* **2022**, *15*, 7055. [[CrossRef](#)]
6. He, X.; Geng, H. Transient stability of power systems integrated with inverter-based generation. *IEEE Trans. Power Syst.* **2020**, *36*, 553–556. [[CrossRef](#)]
7. Shair, J.; Li, H.; Hu, J.; Xie, X. Power system stability issues, classifications and research prospects in the context of high-penetration of renewables and power electronics. *Renew. Sustain. Energy Rev.* **2021**, *145*, 111111. [[CrossRef](#)]
8. Huang, R.; Gao, W.; Fan, R.; Huang, Q. A guided evolutionary strategy based static var compensator control approach for inter-area oscillation damping. *IEEE Trans. Ind. Inform.* **2022**, *19*, 2596–2607. [[CrossRef](#)]
9. Huang, R.; Gao, W.; Fan, R.; Huang, Q. Damping inter-area oscillation using reinforcement learning controlled TCSC. *IET Gener. Transm. Distrib.* **2022**, *16*, 2265–2275. [[CrossRef](#)]
10. Hashmy, Y.; Yu, Z.; Shi, D.; Weng, Y. Wide-area measurement system-based low frequency oscillation damping control through reinforcement learning. *IEEE Trans. Smart Grid* **2020**, *11*, 5072–5083. [[CrossRef](#)]
11. Saadatmand, M.; Gharehpetian, G.B.; Moghassemi, A.; Guerrero, J.M.; Siano, P.; Alhelou, H.H. Damping of low-frequency oscillations in power systems by large-scale PV farms: A comprehensive review of control methods. *IEEE Access* **2021**, *9*, 72183–72206. [[CrossRef](#)]
12. Solomon, E.; Khan, B.; Boulkaibet, I.; Neji, B.; Khezami, N.; Ali, A.; Mahela, O.P.; Pascual Barrera, A.E. Mitigating Low-Frequency Oscillations and Enhancing the Dynamic Stability of Power System Using Optimal Coordination of Power System Stabilizer and Unified Power Flow Controller. *Sustainability* **2023**, *15*, 6980. [[CrossRef](#)]
13. Sreedivya, K.; Jeyanthi, P.A.; Devaraj, D. Improved design of interval type-2 fuzzy based wide area power system stabilizer for inter-area oscillation damping. *Microprocess. Microsyst.* **2021**, *83*, 103957. [[CrossRef](#)]
14. Biswal, S.S.; Swain, D.R.; Rout, P.K. Inter-area and intra-area oscillation damping for UPFC in a multi-machine power system based on tuned fractional PI controllers. *Int. J. Dyn. Control* **2022**, *10*, 1594–1612. [[CrossRef](#)]
15. Huang, L.; Coulson, J.; Lygeros, J.; Dörfler, F. Decentralized data-enabled predictive control for power system oscillation damping. *IEEE Trans. Control Syst. Technol.* **2021**, *30*, 1065–1077. [[CrossRef](#)]
16. Prakash, A.; Kumar, K.; Parida, S. Energy capacitor system based wide-area damping controller for multiple inter-area modes. *IEEE Trans. Ind. Appl.* **2022**, *58*, 1543–1553. [[CrossRef](#)]
17. Alalwani, S.; Isik, S.; Bhattacharya, S. In Inter-area Oscillation Damping Controller for DFIG based Wind Power Plants. In Proceedings of the 2022 IEEE Energy Conversion Congress and Exposition (ECCE), Detroit, MI, USA, 9–13 October 2022; pp. 1–6.
18. Ahmed, F.; Foley, A.; McLoone, S.; Best, R.J.; Cameron, C.; Al Kez, D. Dynamic grid stability in low carbon power systems with minimum inertia. *Renew. Energy* **2023**, *210*, 486–506. [[CrossRef](#)]
19. Eberlein, S. *Small-Signal Stability Modelling and Optimization of Microgrids*; BoD—Books on Demand: Norderstedt, Germany, 2021; Volume 32.
20. Oni, O.E.; Swanson, A.G.; Carpanen, R.P. Small signal stability analysis of a four-machine system with placement of multi-terminal high voltage direct current link. *J. Energy S. Afr.* **2020**, *31*, 73–87. [[CrossRef](#)]
21. Zou, X. *Frequency and Damping Characteristics of Generators in Power Systems*; Virginia Tech: Blacksburg, VA, USA, 2018.
22. Oni, O.E.; Swanson, A.G.; Carpanen, R.P. In Small signal stability analysis of a four machine system with strategic placement of monopolar LCC-HVDC link. In Proceedings of the 2019 Southern African Universities Power Engineering Conference/Robotics and Mechatronics/Pattern Recognition Association of South Africa (SAUPEC/RobMech/PRASA), Bloemfontein, South Africa, 29–31 January 2019; pp. 437–443.
23. Rajapakse, A.D.; Muthumuni, D. In Simulation tools for photovoltaic system grid integration studies. In Proceedings of the 2009 IEEE Electrical Power & Energy Conference (EPEC), Montreal, QC, Canada, 22–23 October 2009; pp. 1–5.
24. Liu, S.; Dougal, R.A. Dynamic multiphysics model for solar array. *IEEE Trans. Energy Convers.* **2002**, *17*, 285–294.
25. Owais, R.; Iqbal, S.J. An Intelligent Two-Level Control of Solar Photovoltaic Power Plant for Electromechanical Oscillation Damping in Power Systems. *Arab. J. Sci. Eng.* **2023**, *48*, 6271–6292. [[CrossRef](#)]
26. Gupta, R.; Gupta, G.; Kastwar, D.; Hussain, A.; Ranjan, H. In Modeling and design of MPPT controller for a PV module using PSCAD/EMTDC. In Proceedings of the 2010 IEEE PES Innovative Smart Grid Technologies Conference Europe (ISGT Europe), Gothenburg, Sweden, 11–13 October 2010; pp. 1–6.
27. Faruque, M.; Zhang, Y.; Dinavahi, V. Detailed modeling of CIGRE HVDC benchmark system using PSCAD/EMTDC and PSB/SIMULINK. *IEEE Trans. Power Deliv.* **2005**, *21*, 378–387. [[CrossRef](#)]

28. Oni, O.E.; Swanson, A.G.; Carpanen, R.P. In Modelling and control of multiterminal LCC HVDC. In Proceedings of the 2018 IEEE PES/IAS PowerAfrica, Cape Town, South Africa, 28–29 June 2018; pp. 274–279.
29. Mankour, M.; Sami, B.S. Mitigation of commutation failure method in LCC converter based on HVDC systems by mean of modeling and simulation. *J. Ambient Intell. Humaniz. Comput.* **2020**, *14*, 5837–5852. [[CrossRef](#)]
30. Peng, J.-H.; Nair, N.-K.; Maryani, A.; Ahmad, A. Adaptive Power System Stabilizer tuning technique for damping inter-area oscillations. In Proceedings of the IEEE PES General Meeting, Minneapolis, MN, USA, 25–29 July 2010; pp. 1–6.
31. Yakout, A.H.; Attia, M.A. In Damping Inter-Area Oscillations Via Weighted Area Signals to PSSs Using TLBO & HS Algorithm. In Proceedings of the 2019 21st International Middle East Power Systems Conference (MEPCON), Cairo, Egypt, 17–19 December 2019; pp. 496–501.
32. Preece, R.; Milanović, J.V.; Almutairi, A.M.; Marjanovic, O. Damping of inter-area oscillations in mixed AC/DC networks using WAMS based supplementary controller. *IEEE Trans. Power Syst.* **2012**, *28*, 1160–1169. [[CrossRef](#)]
33. Patidar, N.; Kolhe, M.; Tripathy, N.; Sahu, B.; Sharma, A.; Nagar, L.; Azmi, A. In Optimized design of wide-area PSS for damping of inter-area oscillations. In Proceedings of the 2015 IEEE 11th International Conference on Power Electronics and Drive Systems, Sydney, Australia, 9–12 June 2015; pp. 1172–1177.
34. Bolzoni, A.; Johansson, N.; Hasler, J. In Modeling the impact of grid-forming E-STATCOMs on inter-area system oscillations. In Proceedings of the 2022 24th European Conference on Power Electronics and Applications (EPE'22 ECCE Europe), Hanover, Germany, 5–9 September 2022; pp. 1–10.
35. Fadhil, S.T.; Vural, A.M. In Comparison of dynamic performances of TCSC, Statcom, SSSC on inter-area oscillations. In Proceedings of the 2018 5th International Conference on Electrical and Electronic Engineering (ICEEE), Istanbul, Turkey, 3–5 May 2018; pp. 138–142.
36. Fayez, M.; Mandor, M.; El-Hadidy, M.; Bendary, F. Fuzzy logic based dynamic braking scheme for stabilization of inter-area. *Acta Electron. Malays. (AEM)* **2019**, *3*, 16–22. [[CrossRef](#)]
37. Fayez, M.; Mandor, M.; El-Hadidy, M.; Bendary, F. Stabilization of inter-area oscillations in two-area test system via centralized interval type-2 fuzzy-based dynamic brake control. *J. Electr. Syst. Inf. Technol.* **2021**, *8*, 1–19. [[CrossRef](#)]
38. Selim, F.; Attia, A.-F. In Power System Stabilizer with Self-Tuning Based on Hierarchical Fuzzy Logic Controller. In Proceedings of the 2022 23rd International Middle East Power Systems Conference (MEPCON), Cairo, Egypt, 13–15 December 2022; pp. 1–6.
39. Sharafi, A.; Vahidnia, A.; Jalili, M. In Application of Consensus Algorithm in Clustering of Distributed Generation Systems for Wide-Area Management and Control. In Proceedings of the 2023 IEEE International Conference on Environment and Electrical Engineering and 2023 IEEE Industrial and Commercial Power Systems Europe (EEEIC/I&CPS Europe), Madrid, Spain, 6–9 June 2023; pp. 1–6.
40. Sharafi, A.; Vahidnia, A.; Jalili, M. In Wide-Area Stabilizing Control using Distributed Generation Systems. In Proceedings of the 2023 11th International Conference on Smart Grid (icSmartGrid), Paris, France, 5–7 June 2023; pp. 1–6.

**Disclaimer/Publisher's Note:** The statements, opinions and data contained in all publications are solely those of the individual author(s) and contributor(s) and not of MDPI and/or the editor(s). MDPI and/or the editor(s) disclaim responsibility for any injury to people or property resulting from any ideas, methods, instructions or products referred to in the content.